Mesoscale induced vertical fluxes over the Iceland-Faroe Ridge

Charly de Marez[1], Angel Ruiz-Angulo[1], and Jonathan Gula [2]

[1]University of Iceland, Reykjavik, Iceland

[2]Laboratoire d'Océanographie Physique et Spatiale (LOPS), University of Brest, CNRS, IRD, Ifremer, IUEM, France

Key Points:

- SWOT altimetry reveals energetic mesoscale eddies on the Iceland-Faroe Ridge
- High-resolution Nnmerical modeling shows these eddies induce intense vertical heat fluxes
- Bottom waters warm, likely due to these fluxes

Corresponding author: Charly de Marez, `charly@hi.is`

Abstract

Mesoscale eddies play a crucial role in ocean dynamics, yet their impact on vertical heat fluxes over topographic features remains poorly understood. This study investigates the Iceland-Faroe Ridge (IFR), a key boundary between the North Atlantic and Nordic Seas, southeast of Iceland. Recent rapid warming in the region has shifted thermal structures, potentially impacting the upper cell of the global thermohaline circulation. Using newly available high-resolution SWOT altimetry and numerical modeling, we directly observe mesoscale turbulence atop the IFR for the first time and quantify its role in driving significant vertical heat fluxes. This turbulence provides a pathway for heat transfer from warming surface waters to the deep Iceland-Scotland Overflow Water, likely contributing to its observed warming over the past four decades. These findings highlight the critical role of mesoscale dynamics in heat redistribution and the need for enhanced monitoring in this climatically sensitive region.

Plain Language Summary

The ocean around Iceland plays a key role in moving heat and shaping the global climate. Small swirling currents, called eddies, help mix ocean heat, but their impact near underwater ridges is not well understood. As ocean temperatures rise rapidly in this region, understanding these processes is crucial. Our study focused on the Iceland-Faroe Ridge, an underwater boundary between the North Atlantic and Nordic Seas. Using new high-resolution satellite data, we observed these swirling currents in detail for the first time and measured how they move heat vertically. We found that these currents create a direct pathway between warming surface waters and colder deep waters below, likely contributing to deep-water warming observed over the past 40 years. This discovery highlights the critical role of these currents in transferring heat and underscores the need for better monitoring to understand how ocean changes will impact climate and marine ecosystems.

1 Introduction

The dynamics of oceanic circulation around Iceland play a critical role in regulating the broader Atlantic Meridional Overturning Circulation (AMOC, Buckley & Marshall, 2016) and, consequently, the global climate system. This region sits at the nexus of warm, saline Atlantic waters flowing northward and cold, fresh Arctic waters moving southward. The complex interactions between these water masses significantly influence heat and freshwater distribution, deep convection, and the stability of AMOC. Understanding these dynamics is essential for predicting the response of high-latitude ocean systems to ongoing climate change (Drijfhout et al., 2012; Winton et al., 2013; Meehl et al., 2014; Lozier et al., 2019; Chafik & Rossby, 2019; Tsubouchi et al., 2021; Brakstad, Gebbie, et al., 2023).

The Iceland-Faroe Ridge (IFR) is a crucial topographic feature within this dynamic region, acting as a natural boundary between the North Atlantic and Nordic Seas. The ridge facilitates complex exchanges of water masses: at the surface, warm Atlantic waters flow northward, and at depth, cold and dense polar waters flows southward atop and around the ridge through the Faroe bank Channel (FBC, Bacon et al., 2022; de Marez et al., 2024). On the one hand, past studies using glider observations proposed that there exists a pathway connecting the surface and the bottom waters there (Beaird et al., 2016). They suggested that the vertical transfers are mainly due to winter convection, mixed layer instability, and deep frontal subduction. On the second hand, it is proven that the ridge also supports the formation of mesoscale eddies (Guo et al., 2014). These latter could play a pivotal role in the vertical redistribution of heat and other tracers. However, the lack of resolution of current altimetry and numerical models hindered a complete analysis of the mesoscale there, and many questions remain regarding the mechanisms by which mesoscale dynamics atop the ridge influence vertical heat fluxes, a key component that could modulate ocean-atmosphere interactions in the area.

This study is timely due to the recent warming of surface waters in the region: along with the rest of the global ocean, the surface waters of the northeastern part of the North Atlantic have been observed to warm in recent decades (Polyakov et al., 2017; Shi et al., 2024). These waters are warming, up to twice as fast as the global average (Pörtner et al., 2019). Specifically, south of Iceland, it is striking that the 9°C annual mean isotherm has shifted northwards to the IFR. In this region, surface waters have become significantly warmer, increasing by about 1°C over the last 40 years (Fig. 1). Rising sea surface temperatures can amplify stratification and alter mesoscale eddy activity, potentially reshaping the dynamics governing vertical heat fluxes. Given the critical role of the IFR region in ocean circulation and climate regulation, it is imperative to assess how these ongoing changes impact heat transfer processes. This study addresses this pressing need by providing new insights into mesoscale eddy dynamics using newly released high resolution altimetry and numerical modeling. We discuss the influence of the mesoscale dynamics on vertical heat fluxes, thereby advancing our understanding of the evolving physical oceanography of the Iceland-Faroe Ridge.

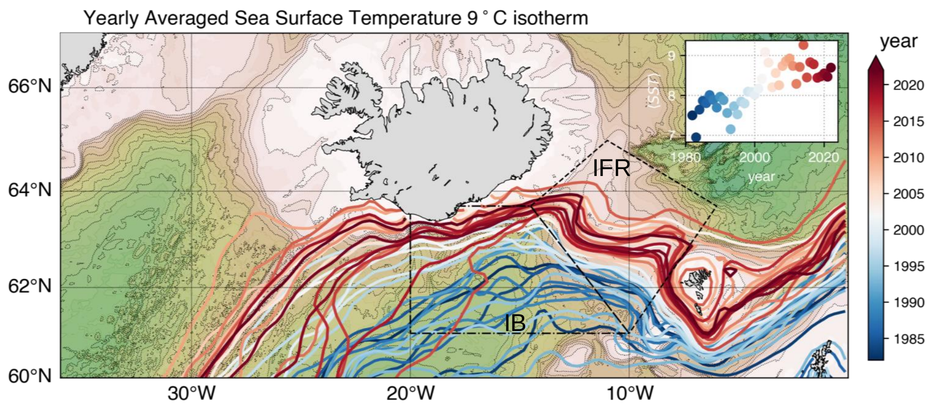

Figure 1. Temporal evolution of the 9°C surface isotherm from yearly averages over the period 1981-2022; the top right insert shows the yearly averaged sea surface temperature over the IFR (dashed lines area).

2 Data and Methods

2.1 SWOT data

We leverage newly released satellite data from the Surface Water and Ocean Topography (SWOT), a collaborative effort between NASA and CNES launched in late 2022, to unveil unprecedented details of surface mesoscale geostrophic turbulence over the IFR (Morrow et al., 2019). Specifically, we use the SWOT_L3_SSH product, derived from the L2 SWOT KaRIn Low rate ocean data products provided by NASA/JPL and CNES. This dataset is produced and freely distributed by the AVISO and DUACS teams as part of the DESMOS Science Team project (AVISO/DUACS, 2023). The "noise-reduced" Sea Level Anomaly (SLA), displayed on a 2-km resolution grid, is used for our analysis (Fig. 2b, see Dibarboure et al., 2023, for details on the method). This allows the computation of instantaneous geostrophic velocities (u_{swot}, see Fig. 2c) and normalized relative vorticity (ζ/f, Fig. 2d). It is important to note that the denoising of the SLA during the noise reduction reduces the energy level of the observed structures. The SLA from SWOT is compared with SLA data from a 1/8° gridded product provided by AVISO on the same day (Fig. 2a). The two-dimensional data provided by SWOT, without further interpolation, offers a more accurate estimate of the horizontal structure of surface ocean currents for the first time. Recent studies (X. Zhang et al., 2024; Z. Zhang et al., 2024; Verger-Miralles et al., 2024; Du & Jing, 2024; Damerell et al., 2025; Wang et al., 2025; Tchilibou et al., 2025; Carli et al., 2025) unveiled the SWOT's ability to resolve small eddies, revealing structures of smaller extent than those detected in gridded altimetric products (using a detection algorithm, here *py-eddy-tracker,* Mason et al., 2014).

We use data from the 1-day repeat orbit phase spanning the period 03/29/2023-07/08/2023 to compute the average Eddy Kinetic Energy $\langle EKE\rangle$. This is calculated as $\langle EKE\rangle = \langle\frac{1}{2}({u'_{\mathrm{swot}}}^2 + {v'_{\mathrm{swot}}}^2)\rangle$, where $u'_{\mathrm{swot}} = u_{\mathrm{swot}} - \langle u_{\mathrm{swot}}\rangle$, with u and v being the instantaneous velocities and $\langle\cdot\rangle$ denoting a temporal average over the entire period. This allows for the first time to provide a synoptic estimate of the mesoscale activity on the IFR. Note that the denoising procedure in SWOT data smoothen SSH gradients, and therefore reduces the energy of the signal (Dibarboure et al., 2023).

2.2 GIGATL1 simulation

We use outputs from a realistic numerical simulation conducted as part of the GIGATL set of Atlantic Ocean simulations (Gula et al., 2021), using the Coastal and Regional Ocean COmmunity model (CROCO), a version of the ROMS model (Shchepetkin & McWilliams, 2005). This model solves the hydrostatic primitive equations using the full equation of state for seawater (Shchepetkin & McWilliams, 2011). Specifically, we use the GIGATL1 version with a horizontal resolution of 1 km and 100 terrain-following levels, which allows resolution of mesoscale dynamics on the IFR. The simulation is initialized in July 2007 using outputs from the GIGATL3 simulation, which has a 3 km horizontal resolution and is initialized with the Simple Ocean Data Assimilation (SODA) (Carton & Giese, 2008) and spun up for 3 years. Boundary conditions are provided by SODA, while the simulation is forced with hourly atmospheric forcing from the Climate Forecast System Reanalysis (CFSR) (Saha et al., 2010), using a bulk formulation with relative winds (Renault et al., 2020). Tidal effects are included, with barotropic tidal forcing at the boundaries and tidal potential and self-attraction taken from TPXO7.2 and GOT99.2b, respectively. Bathymetry data are obtained from the SRTM30plus dataset (Becker et al., 2009). The k-ϵ turbulence closure scheme is used for vertical mixing parameterization, with the Canuto A stability function formulation applied. No explicit lateral diffusivity is included in the simulation. Bottom friction effects are parameterized using a logarithmic law of the wall with a roughness length of 0.01 m. For this study, we use daily averages to remove the tidal signature, covering a 1-year period to capture a full seasonal cycle. Quantities averaged over this seasonal cycle are denoted as $\langle\cdot\rangle$. The EKE from GIGATL1 output is computed using the same definition as for the SWOT data. Previous studies leveraging the GIGATL ensemble have discussed and validated these simulations extensively (Ruan et al., 2021; Barkan et al., 2021; Qu et al., 2021; Mashayek et al., 2021; Vic et al., 2022; Uchida et al., 2022; Tagliabue et al., 2022; Schubert et al., 2023; Napolitano et al., 2024).

From the GIGATL1 outputs, the turbulent vertical kinematic heat flux (VHF = $C_{\mathrm{p}}\rho_0 w'T'$, see *e.g.,* McPhee, 1992; McPhee & Martinson, 1994; Su et al., 2018) is computed along designated vertical sections. C_{p} is the specific heat capacity of sea water and ρ_0 is the average density of sea water. The vertical velocity w and temperature T are low-pass filtered to remove the influence of internal waves. The filter is a 4th-order Butterworth filter with a cutoff frequency of one week. Then, anomalies are computed as

$w' = w^* - \langle w \rangle_{\text{month}}$ and $T' = T^* - \langle T \rangle_{\text{month}}$, where $\cdot^*$ denotes the filtered quantities, and $\langle \cdot \rangle_{\text{month}}$ are monthly averages. This procedure ensures that only the influence of mesoscale structures is considered, and takes into account the seasonal variations of temperature on the vertical.

To study the nature of the instabilities responsible for the generation of mesoscale structures on the IFR, we compute energy transfers from the GIGATL1 outputs in the same fashion as in *e.g.,* Gula et al. (2016). Assuming that the flow can be decomposed as $u = \langle u \rangle_{\text{month}} + u'$, the transfer from the Mean Kinetic Energy (MKE) to the kinetic energy of the perturbation (the EKE) can be expressed as:

$$\mathcal{T}_{\text{MKE}\rightarrow\text{EKE}} = HRS + VRS, \tag{1}$$

where

$$HRS = -\langle u'^2 \rangle \partial_x \langle u \rangle - \langle u'v' \rangle \partial_y \langle u \rangle - \langle v'^2 \rangle \partial_y \langle v \rangle - \langle u'v' \rangle \partial_x \langle v \rangle, \tag{2}$$

is the contribution from the Horizontal Reynolds Stress (the suscript $\cdot_{\text{month}}$ has been omitted for simplicity here), and

$$VRS = -\langle u'w' \rangle \partial_z \langle u \rangle - \langle v'w' \rangle \partial_z \langle v \rangle, \tag{3}$$

is the contribution of the Vertical Reynolds Stress. Second, the transfer from the Potential Energy (PE) of the perturbation to the EKE is the Vertical Buoyancy Flux:

$$\mathcal{T}_{\text{PE}\rightarrow\text{EKE}} = VBF = \langle w'b' \rangle. \tag{4}$$

The transfer terms shown in Fig. S1 are then averaged over a full seasonal cycle and integrated vertically.

Finally, we conduct offline 3D particle advection simulations using the Python code *Pyticles*, which is specifically designed for CROCO model outputs. The code source and a comprehensive list of studies using this tool are available at `https://github.com/Mesharou/Pyticles`. In these simulations, particles are initially seeded within a 500×500 km box centered at 11°W, 63.5°N, with 10 km spacing on the 80th and 90th vertical levels (close to the surface). The advection simulation we show spans 5 months, starting in November, with particles continuously injected each month, resulting in a total of 24,670 particles. Additional simulations with different seeding periods were conducted (not shown here) and showed no conceptual differences from the results presented in this study.

2.3 *in situ* measurements around Iceland

The Sea Surface Temperature (SST) measurements shown in Fig. 1 are from NOAA/NCEI 1/4° Daily Optimum Interpolation Sea Surface Temperature (OISST), Version 2.1 (Banzon et al., 2014).

The ocean current velocity data shown in Fig. 4c were collected during the 2021 NORSE pilot cruise aboard the R/V Armstrong. The plot shows the combined shipboard ADCP WH300 kHz and OS38 kHz. The derived velocities are obtained using the UHDAS toolbox (Firing & Hummon, 2010).

The *in situ* temperature and salinity (T/S) data in the period 1980-2020 shown in Fig. 5 are part of the SDC_ARC_DATA_TS_V2 dataset and the Norwegian Marine Data Center (Brakstad, Våge, et al., 2023). The total number of data points used for the histograms are 118847, 40908, and 73989, in the range $1 < \mathrm{CT} < 6°\mathrm{C}$ and $35 < \mathrm{SA} < 35.4\,\mathrm{g\,kg^{-1}}$. The profiles used cover the area along the Icelandic shelf, and thus sample ISOW. We extended the study area down to 61 °N as the ISOW signature can be found even far from the shelf.

3 Results

3.1 Unveiling the mesoscale turbulence on top the IFR

Novel high-resolution satellite altimetry data reveal the presence of highly turbulent flow characterized by numerous mesoscale structures atop the IFR. The relatively small horizontal size of mesoscale eddies in this region, determined by the first baroclinic Rossby deformation radius being on the order of 10 km (Chelton et al., 1998), has previously hindered the detailed analysis of mesoscale activity. For example, eddies detected on the IFR in classical gridded-altimetry products (Fig. 2a) have diameters of $\mathcal{O}(100)$ km.

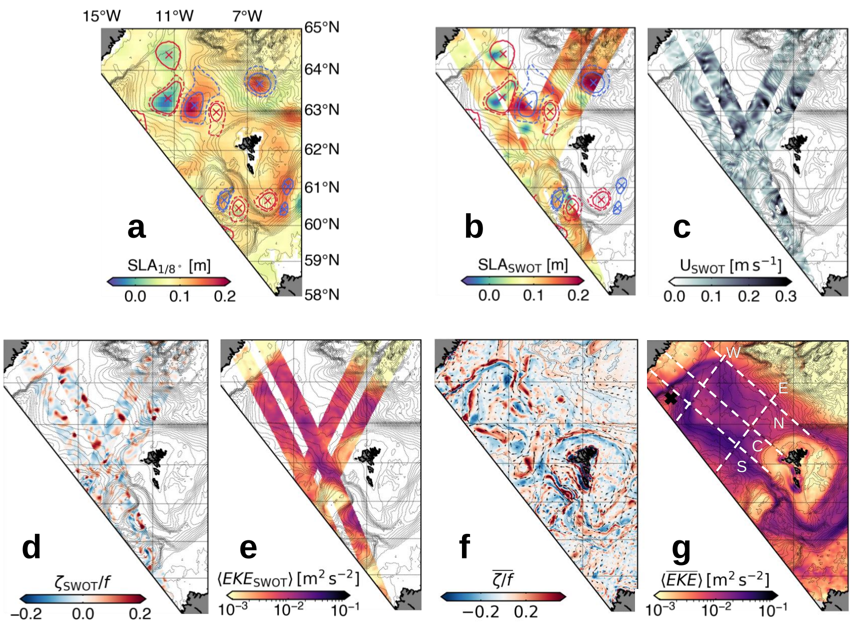

Figure 2. a, Snapshot of SLA from from 1/8° gridded altimetry on 06/10/2023, and contours of cyclonic (red) and anticyclonic (blue) mesoscale eddies using the *py-eddy-tracker* algorithm. b, SWOT KaRIn 2-km resolution noiseless SLA in passes #5 and #16 on 06/10/2023; the eddy detection from the gridded product is superimposed. c, Geostrophic velocity magnitude derived from SWOT SLA. d, Normalized relative vorticity estimated from SWOT-derived geostrophic currents. e, Eddy Kinetic Energy estimated from SWOT-derived geostrophic currents, averaged over the period 03/29/2023-07/08/2023. f, Normalized relative vorticity, averaged vertically, estimated from GIGATL1 outputs, on 06/25/2008 —note the different color range in d and f. g, Eddy Kinetic Energy estimated from GIGATL1 simulation outputs, averaged vertically and over one seasonal cycle.

However, the reality differs significantly: the SLA measurements from SWOT altimetry on the same day reveal unprecedented details of the SLA field (Fig. 2b) and demonstrate that classical altimetry misrepresents eddies in this region. A striking example is the cyclonic eddy located at $\sim 12°$W, 63.3°N, which is 2 to 3 times smaller in the SWOT observation compared to AVISO. The same applies to the cyclonic eddy further north at $\sim$ 12°W, 64.5°N. Antoher example is a small cyclone located at $\sim$ 10°W, 62.5°N, only seen in SWOT data and not visible in the AVISO product.

The noise-reduced SWOT data enable the computation of geostrophic currents (Fig. 2c) and relative vorticity (Fig. 2d). The latter highlights the numerous $\mathcal{O}(10)$ km radius mesoscale eddies, previously unobservable with classical altimetry, but now captured synoptically by SWOT. These eddies are responsible for an intense turbulent flow over the IFR. This turbulence is concentrated on the IFR, as evidenced by higher values of mean EKE over the IFR compared to, for instance, the region north of it (Fig. 2e).

A high-resolution, realistic numerical simulation further enables a comprehensive study of this mesoscale turbulence. The GIGATL1 simulation reproduces the turbulence observed in SWOT with remarkable accuracy. (i) In terms of the relative vorticity field, although the ζ/f values are more intense in the simulation than in SWOT (mainly due to the noise removal procedure in SWOT), the diameters of the eddies—represented by vorticity patches—are comparable in SWOT and GIGATL1 (see Fig. 2d,f). (ii) In terms of EKE, the order of magnitude in both SWOT and GIGATL1 is similar, with high values concentrated in the same locations (see Fig. 2e,g).

The GIGATL1 simulation also provides access to 3D fields and facilitates advanced diagnostics such as energy transfer terms (see Methods, Section 2). These terms are, on average, positive at the position of a jet located in the western valley of the IFR (see Fig. S1). The observed mesoscale eddies thus originate from barotropic and baroclinic instabilities of this jet, which effectively acts as an "eddy shotgun." This can be noticed, for example, in the relative vorticity field (Fig. 2f). The eddies subsequently propagate southeastward along the ridge, driven by topographic Rossby waves (de Marez et al., 2017), populating the IFR with coherent structures.

3.2 Impact of the mesoscale turbulence on vertical motions

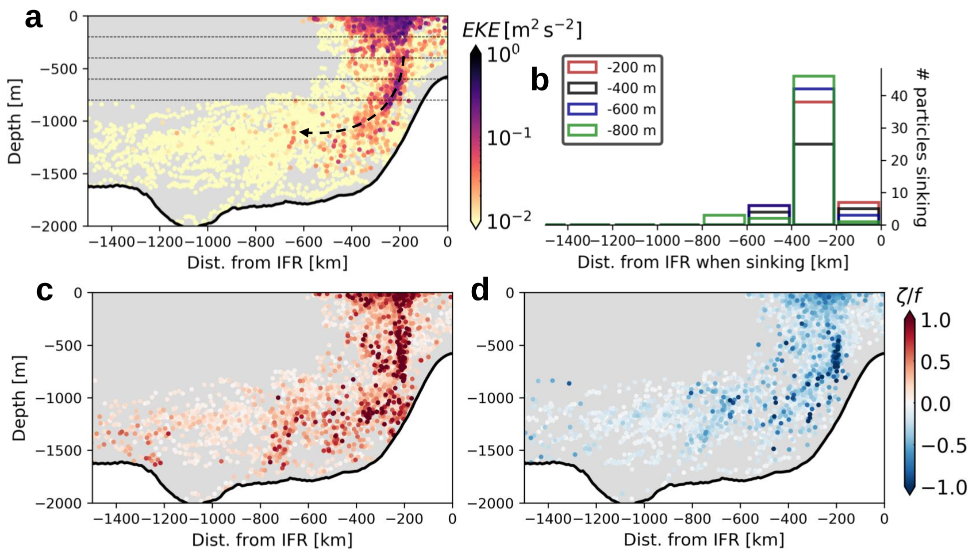

Figure 3. a, Across-ridge cumulative section of EKE of particles advected in GIGATL1 outputs; the position of particles is presented as their depth *vs.* their distance from the IFR (with negative value meaning South of the IFR); the bold line shows the along-slope averaged topography. b, Histogram showing the distance from the IFR at which particles sank below 4 selected depths: 200,400, 600 and 800 m, shown by the dotted lines in panel a. c,d, Same as panel a but for normalized particle relative vorticity (c, positive, d, negative).

The high-resolution realistic numerical simulation unveils the impact of mesoscale turbulence on the vertical transport of tracers—particularly temperature—from the surface down to the bottom layer. This vertical transport can be qualitatively illustrated by seeding particles in the simulation at the surface and running 3D particle advection schemes (see Methods, Section 2). We extract the particles that were seeded in the open ocean (excluding those from the continental shelf) and completed their journeys south of the IFR at depths below 500 m. The points in the scatter plots of Fig. 3 correspond to the cumulative section of the positions of all these specific particles at all timesteps of the simulations. We estimate the EKE and the normalized relative vorticity of the particles by extracting the values from the GIGATL1 outputs at the corresponding grid points. The analysis reveals that when seeded at the surface, the particles reaching the ocean bottom south of the IFR experience high EKE values along their paths (Fig. 3a). Most of the particles sink near the IFR, at a distance between 200 and 400 km south of its shallowest part (Fig. 3b). They also encounter high values of relative vorticity (Fig. 3c,d).

This shows that sinking water parcels south of the IFR are likely influenced by mesoscale turbulence during their descent.

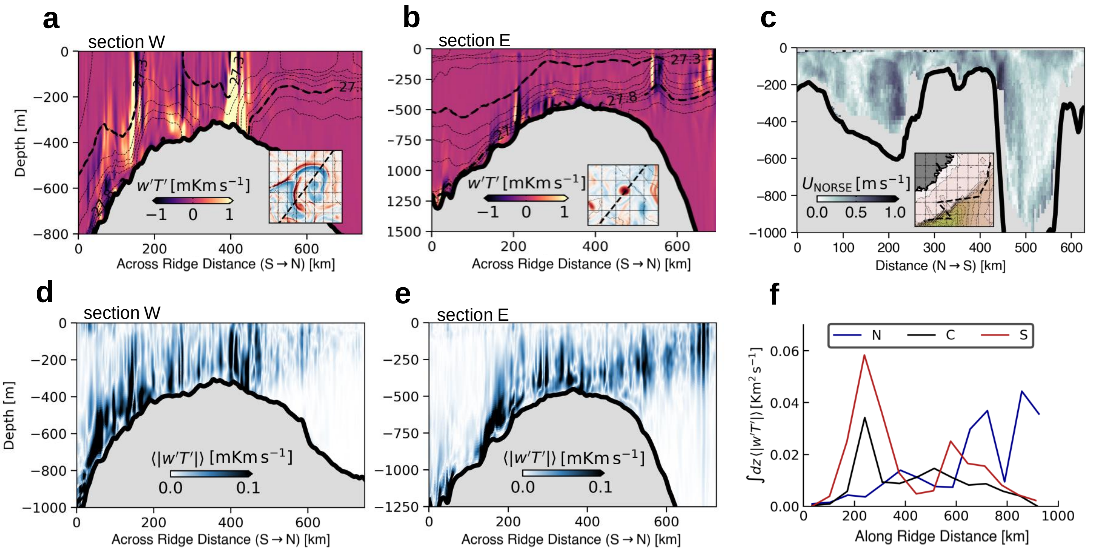

Figure 4. a, Snapshot of $w'T'$ along the section labeled W in Fig. 2g, from south to north; the dashed lines show isopycnals with a 0.1 $\mathrm{kg\,m^{-3}}$ spacing; the inset shows the surface relative vorticity at the time of the section, with the same colormap as in panel d and the position of the section. b, Same as panel a along the section labeled E in panel Fig. 2g. c, Along track section of the currents speed from the NORSE cruise over the IFR's Western Valley; the insert shows the bathymetry and the position of the section. d, (resp. e) $\langle |w'T'| \rangle$ (time average) along the section labeled E (resp. W) in panel b. f, Vertically-integrated average Vertical Heat Flux magnitude along the sections labeled N, C, and S in Fig. 2g.

More specifically, diagnostics from the high-resolution realistic numerical simulation show that mesoscale turbulence induces vertical fluxes of temperature from the surface down to the bottom layer. The turbulent vertical kinematic heat flux (or Vertical Heat Flux, VHF $= C_{\mathrm{p}}\rho_0 w'T'$, see Methods, Section 2) generated by individual mesoscale events reaches magnitudes exceeding $10^3\,\mathrm{W\,m^{-2}}$. As a first example, the bottom-reaching jet located in the western valley of the IFR—referred to as the "eddy shotgun"—which often deflects eastward to form an anticyclonic gyre, produces intense VHF from the surface to the seafloor (Fig. 4a,c). As a second example, coherent surface-intensified eddies, formed remotely by the eddy shotgun, extend down to the bottom layer. The VHF associated with these eddies is observed to penetrate the $\sigma_0 = 27.8, \mathrm{kg}, \mathrm{m}^{-3}$ isopycnal (Fig. 4b).

Therefore, quantitatively, there is an intense eddy-driven transfer of heat toward the bottom atop the IFR. On average, the VHF over the IFR displays a clear pathway from the surface to the bottom, with a magnitude of $\mathcal{O}(10^2)\,\mathrm{W\,m^{-2}}$ (Fig. 4d,e). These values are consistent with *in situ* observations (Thompson et al., 2016) and estimates from other high-resolution numerical simulation analyses (Su et al., 2018). They are 10 times larger than the mesoscale vertical heat transport observed in most regions of the ocean (Su et al., 2018), comparable in magnitude to air-sea heat fluxes (Large & Yeager, 2009), and persist throughout the entire seasonal cycle. This highlights the predominance of eddy-induced heat flux compared to convection-induced heat flux, which occurs only during winter (Su et al., 2018). Peak values exceeding $10^3\,\mathrm{W\,m^{-2}}$ are observed at two major vertical heat transfer hotspots: one located on the western side of the ridge and the other on the eastern side, where remotely generated eddies accumulate (Fig. 4f).

This intense VHF is also evident at the ocean floor, where currents flow along the topography (see Fig. S2). In particular, on the southern flank of the IFR, a bottom current described by de Marez et al. (2024) generates bottom-intensified vortices through intrinsic barotropic and baroclinic instabilities (Guo et al., 2014). These vortices produce bottom-intensified VHF, which thickens the bottom mixed layer connecting the seafloor with the ocean interior, similar to what has been observed in past *in situ* measurements (Fer et al., 2010; de Marez et al., 2024).

4 Discussion on the fate of ISOW

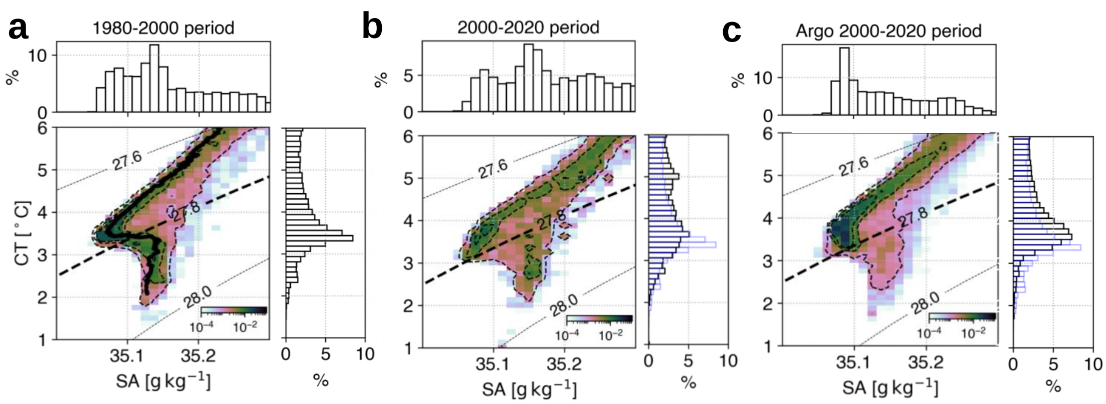

Figure 5. a (resp. b), 2D histogram (the color represents the percentage of datapoints relative to the total of points in the TS diagram) of temperature and salinity shipboard hydrographic data over the period 1980-2000 (resp. 2000-2020) in the Iceland Basin (IB, dot-dashed lines area in Fig. 1); black line in b shows a particular cast from Saunders (1996) presenting the historical "chair-like" profile of the ISOW; inserts show cumulative histograms over salinity and temperature. c, same as a,b from Argo floats data in the same area for the period 2000-2020. Blue bars plots in inserts of panels b,c recall the cumulative histogram for temperature in the period 1980-2000.

South of Iceland, at depth, cold waters formed in the Nordic Seas overflow into the North Atlantic through the IFR and the FBC (Bacon et al., 2022), carried by bottom currents flowing along the IFR and downstream south of Iceland (de Marez et al., 2024). This bottom water mass is called the Iceland-Scotland Overflow Water (ISOW, Kanzow & Zenk, 2014; Zou et al., 2017, 2020; Johns et al., 2021). It has been described as the main contributor to the lower limb of AMOC (Dickson & Brown, 1994; Sarafanov et al., 2012) with about 5.3 Sv leaving the Iceland Basin (from 4 years of moored observations, see Johns et al., 2021). It is typically defined as the water mass below the $\sigma_0 = 27.8\,\mathrm{kg\,m^{-3}}$ isopycnal (Bowles & Jahn, 1983; Hansen, 1985; Perkins et al., 1998; Hansen & Østerhus, 2000; Fogelqvist et al., 2003; Hansen & Østerhus, 2007; Beaird et al., 2013; Logemann et al., 2013; Guo et al., 2014; Ullgren et al., 2014; Daniault et al., 2016; Zou et al., 2017; Zhao et al., 2018; Hansen et al., 2018; Petit et al., 2019; Chafik & Rossby, 2019; Koman et al., 2022; Brakstad, Gebbie, et al., 2023; Devana & Johns, 2024). This water mass used to have a clear —historical— T/S signature (Saunders, 1996, and Fig. 5a), which can be observed far downstream throughout the subpolar gyre (Van Aken & Becker, 1996).

A compilation of all available data collected where the ISOW overflows south of Iceland, in the Iceland Basin (IB, see definition in Fig. 1), provides compelling evidence of significant changes over the last 40 years, with a temperature increase of approximately $\sim 0.5°$C (Fig. 5b,c). This is consistent with the observed warming of bottom temperatures in the FBC, monitored by a mooring array and quantified at 0.1 °C per decade by Larsen et al. (2024). The mechanisms potentially responsible for the ISOW warming are limited and can be narrowed down to two main processes.

First, assuming no mixing with ambient water during its transit, the T/S properties of ISOW should remain unchanged between its formation site (the Greenland Sea, see Brakstad, Gebbie, et al., 2023) and the measurement site (here south of Iceland). In the Greenland Sea, profound changes in surface temperatures are occurring (see Section 3 of the Supporting Information). This suggests that the first plausible cause of ISOW warming south of Iceland originates in the far-field. This hypothesis aligns with findings from Strehl et al. (2024), who documented the warming of deep water formed in the Greenland Sea, and with the conclusions of Larsen et al. (2024), who recently proposed that the warming of overflow bottom water observed in the FBC originates further north of the IFR.

Second, as ISOW flows from its generation site to the North Atlantic, the IFR is the only location where it is sufficiently close to surface waters (Beaird et al., 2016) to be influenced by surface warming at a location other than its formation site (Fig. 1). At this critical location, our study highlights strong mesoscale turbulence-induced VHF, revealed through both SWOT altimetry and high-resolution numerical simulations. This turbulence creates a direct pathway between the warming surface waters (Fig. 1) and the ISOW layer (Fig. 4). This observation aligns with previous glider data suggesting subduction of the Iceland-Faroe Front atop the IFR (Beaird et al., 2016). We show here that the mesoscale turbulence is likely facilitating this subduction, and therefore facilitating heat transfer from the surface to the bottom to finally contribute to the observed warming of ISOW.

5 Conclusion

These results suggest that in a warmer future with potentially increased mesoscale activity (Martínez-Moreno et al., 2021; Beech et al., 2022; Barceló-Llull et al., 2024), the deepest branch of the AMOC overflowing in the North Atlantic may become warmer, thus affecting the global properties of water masses in the global ocean. In particular, with the observed temperature increase over the past 40 years, coupled with IPCC projections (Pörtner et al., 2019), it is plausible that bottom water temperatures could increase by 1-3°C by the end of the century. The current lack of comprehensive *in situ* data and time coverage in high-resolution numerical simulations limits stronger evidence for the mechanisms proposed here. This work, therefore, serves as an alert, identifying a possible early warning hotspot for tipping points and emphasizing the need for timely monitoring of changes in bottom water properties, as these will impact benthic species populations and global ocean circulation.

Acknowledgments

C.d.M. was supported by a Queen Margrethe II´s and Vigdís Finnbogadóttir's Interdisciplinary Research Centre on Ocean, Climate and Society (ROCS) postdoctoral fellowship. A.R.A. was supported by ROCS. Simulations were performed using the HPC facilities DATARMOR of 'Pôle de Calcul Intensif pour la Mer' at Ifremer, Brest, France. We would like to acknowledge the significant effort invested in acquiring and maintaining the Hydrography Observational Programme by the Icelandic Marine and Freshwater Research Institute. Additional computer resources and research IT are provided by UTS of the University of Iceland through the Icelandic research e-Infrastructure project (IREI), funded by the Icelandic Infrastructure Fund.

Open Research

SWOT data and gridded-altimetry data can be downloaded on AVISO website `https://www.aviso.altimetry.fr/en/my-aviso-plus.html`. *in situ data* are provided by the SeaDataNet Pan-European infrastructure for ocean and marine data management (`https://www.seadatanet.org`), and can be downloaded as part of the SDC_ARC_DATA_TS_V2 dataset and the Norwegian Marine Data Center (Brakstad, Våge, et al., 2023). Due to the large size of simulation outputs, they are available upon request.

Historical data from Saunders (1996) are accessible *via* the MEDIN portal (`https://portal.medin.org.uk`), which collects marine data across UK organisations. The Argo floats data are available on the Coriolis website (`www.coriolis.eu.org`). Satellite measurements of temperature can be downloaded using NOAA download services at `https://www.ncei.noaa.gov/data/sea-surface-temperature-optimum-interpolation/`. The ocean current velocity data were collected during the 2021 NORSE pilot cruise aboard the R/V Armstrong, and they are available following UCSD's portal `http://www.mod.ucsd.edu/norse`.

References

AVISO/DUACS. (2023). SWOT Level-3 SSH Basic (v0.3) [Data set]. doi: 0.24400/527896/A01-2023.017

Bacon, S., Garabato, A. C. N., Aksenov, Y., Brown, N. J., & Tsubouchi, T. (2022). Arctic ocean boundary exchanges. *Oceanography*, *35*(3/4), 94–102.

Banzon, V. F., Reynolds, R. W., Stokes, D., & Xue, Y. (2014). A 1/4-spatial-resolution daily sea surface temperature climatology based on a blended satellite and in situ analysis. *Journal of Climate*, *27*(21), 8221–8228.

Barceló-Llull, B., Rosselló, P., Combes, V., Sánchez-Román, A., Pujol, M. I., & Pascual, A. (2024). Robust intensification of global ocean Eddy Kinetic Energy from three decades of satellite altimetry observations. *arXiv preprint arXiv:2406.08014*.

Barkan, R., Srinivasan, K., Yang, L., McWilliams, J. C., Gula, J., & Vic, C. (2021). Oceanic mesoscale eddy depletion catalyzed by internal waves. *Geophysical Research Letters*, *48*(18), e2021GL094376.

Beaird, N., Rhines, P., & Eriksen, C. (2013). Overflow waters at the Iceland–Faroe Ridge observed in multiyear seaglider surveys. *Journal of Physical Oceanography*, *43*(11), 2334–2351.

Beaird, N., Rhines, P., & Eriksen, C. (2016). Observations of seasonal subduction at the iceland-faroe front. *Journal of Geophysical Research: Oceans*, *121*(6), 4026–4040.

Becker, J. J., Sandwell, D. T., Smith, W. H. F., Braud, J., Binder, B., Depner, J., ... Weatherall, P. (2009, November). Global Bathymetry and Elevation Data at 30 Arc Seconds Resolution: SRTM30_plus. *Marine Geodesy*, *32*(4), 355–371. doi: 10.1080/01490410903297766

Beech, N., Rackow, T., Semmler, T., Danilov, S., Wang, Q., & Jung, T. (2022). Long-term evolution of ocean eddy activity in a warming world. *Nature climate change*, *12*(10), 910–917.

Bowles, F. A., & Jahn, W. H. (1983). Geological/geophysical observations and inferred bottom-current flow: South flank Iceland—Faeroe Ridge. *Marine Geology*, *52*(3-4), 159–185.

Brakstad, A., Gebbie, G., Våge, K., Jeansson, E., & Ólafsdóttir, S. R. (2023). Formation and pathways of dense water in the Nordic Seas based on a regional inversion. *Progress in Oceanography*, *212*, 102981.

Brakstad, A., Våge, K., Ólafsdóttir, S. R., Jeansson, E., & Gebbie, G. (2023). Hydrographic and geochemical observations in the nordic seas between 1950 and 2019. , 102981. doi: 10.21335/NMDC-1271328906

Buckley, M. W., & Marshall, J. (2016). Observations, inferences, and mechanisms of the Atlantic Meridional Overturning Circulation: A review. *Reviews of Geophysics*, *54*(1), 5–63.

Carli, E., Tranchant, Y., Siegelman, L., Le Guillou, F., Morrow, R. A., Ballarotta, M., & Vergara, O. (2025). Small-scale eddy diagnostics around the Southern Ocean Polar Front with SWOT. *Authorea Preprints*.

Carton, J. A., & Giese, B. S. (2008, August). A Reanalysis of Ocean Climate Using Simple Ocean Data Assimilation (SODA). *Monthly Weather Review*, *136*(8), 2999–3017. doi: 10.1175/2007MWR1978.1

Chafik, L., & Rossby, T. (2019). Volume, heat, and freshwater divergences in the subpolar North Atlantic suggest the Nordic Seas as key to the state of the meridional overturning circulation. *Geophysical Research Letters*, *46*(9), 4799–4808.

Chelton, D. B., deSzoeke, R. A., Schlax, M. G., El Naggar, K., & Siwertz, N. (1998, March). Geographical Variability of the First Baroclinic Rossby Radius of Deformation. *Journal of Physical Oceanography*, *28*(3), 433–460. doi: 10.1175/1520-0485(1998)028<0433:GVOTFB>2.0.CO;2

Damerell, G. M., Bosse, A., & Fer, I. (2025). Merging of a mesoscale eddy into the Lofoten Vortex in the Norwegian Sea captured by an ocean glider and SWOT observations. *EGUsphere*, *2025*, 1–28.

Daniault, N., Mercier, H., Lherminier, P., Sarafanov, A., Falina, A., Zunino, P., ... others (2016). The northern North Atlantic Ocean mean circulation in the early 21st century. *Progress in Oceanography*, *146*, 142–158.

de Marez, C., Carton, X., Morvan, M., & Reinaud, J. N. (2017). The interaction of two surface vortices near a topographic slope in a stratified ocean. *Fluids*, *2*(4), 57.

de Marez, C., Ruiz-Angulo, A., & Le Corre, M. (2024). Structure of the bottom boundary current South of Iceland and spreading of deep waters by submesoscale processes. *Geophysical Research Letters*, *51*(5), e2023GL107508.

Devana, M., & Johns, W. (2024). Structure and variability of iceland scotland overflow water transport in the western iceland basin. *Journal of Geophysical Research: Oceans*, *129*(8), e2023JC020107.

Dibarboure et al. (2023). *SWOT Level-3 Overview algorithms and examples.* https://swotst.aviso.altimetry.fr/fileadmin/user_upload/SWOTST2023/postersPI/faugere_ocean_l3_PIproject.pdf. (Poster at SWOT Science Team 2023)

Dickson, R. R., & Brown, J. (1994). The production of North Atlantic Deep Water: sources, rates, and pathways. *Journal of Geophysical Research: Oceans*, *99*(C6), 12319–12341.

Drijfhout, S., Van Oldenborgh, G. J., & Cimatoribus, A. (2012). Is a decline of AMOC causing the warming hole above the North Atlantic in observed and modeled warming patterns? *Journal of Climate*, *25*(24), 8373–8379.

Du, T., & Jing, Z. (2024). Fine-scale eddies detected by swot in the kuroshio extension. *Remote Sensing*, *16*(18), 3488.

Fer, I., Voet, G., Seim, K. S., Rudels, B., & Latarius, K. (2010). Intense mixing of the faroe bank channel overflow. *Geophysical Research Letters*, *37*(2).

Firing, E., & Hummon, J. (2010). Shipboard adcp measurements.

Fogelqvist, E., Blindheim, J., Tanhua, T., Østerhus, S., Buch, E., & Rey, F. (2003). Greenland–Scotland overflow studied by hydro-chemical multivariate analysis. *Deep Sea Research Part I: Oceanographic Research Papers*, *50*(1), 73–102.

Gula, J., Molemaker, M. J., & McWilliams, J. C. (2016). Topographic generation of submesoscale centrifugal instability and energy dissipation. *Nature communications*, *7*(1), 12811.

Gula, J., Theetten, S., Cambon, G., & Roullet, G. (2021, June). *Description of the gigatl simulations.* Zenodo. Retrieved from https://doi.org/10.5281/zenodo.4948523 doi: 10.5281/zenodo.4948523

Guo, C., Ilicak, M., Fer, I., Darelius, E., & Bentsen, M. (2014). Baroclinic instability of the Faroe Bank Channel overflow. *Journal of Physical Oceanography*, *44*(10), 2698–2717.

Hansen, B. (1985). The circulation of the northern part of the Northeast Atlantic. *Rit. Fisk.*, *9*, 110–126.

Hansen, B., Larsen, K. M. H., Olsen, S. M., Quadfasel, D., Jochumsen, K., & Østerhus, S. (2018). Overflow of cold water across the Iceland–Farœ Ridge through the Western Valley. *Ocean Science*, *14* (4), 871–885.

Hansen, B., & Østerhus, S. (2000). North atlantic–nordic seas exchanges. *Progress in oceanography*, *45* (2), 109–208.

Hansen, B., & Østerhus, S. (2007). Faroe bank channel overflow 1995–2005. *Progress in Oceanography*, *75* (4), 817–856.

Johns, W. E., Devana, M., Houk, A., & Zou, S. (2021). Moored observations of the Iceland-Scotland overflow plume along the eastern flank of the Reykjanes Ridge. *Journal of Geophysical Research: Oceans*, *126* (8), e2021JC017524.

Kanzow, T., & Zenk, W. (2014). Structure and transport of the Iceland Scotland Overflow plume along the Reykjanes Ridge in the Iceland Basin. *Deep Sea Research Part I: Oceanographic Research Papers*, *86*, 82–93.

Koman, G., Johns, W., Houk, A., Houpert, L., & Li, F. (2022). Circulation and overturning in the eastern North Atlantic subpolar gyre. *Progress in oceanography*, *208*, 102884.

Large, W., & Yeager, S. (2009). The global climatology of an interannually varying air–sea flux data set. *Climate dynamics*, *33*, 341–364.

Larsen, K. M. H., Hansen, B., Hátún, H., Johansen, G. E., Østerhus, S., & Olsen, S. M. (2024). The Coldest and densest overflow branch into the North Atlantic is stable in transport, but warming. *Geophysical Research Letters*, *51* (16), e2024GL110097.

Logemann, K., Ólafsson, J., Snorrason, Á., Valdimarsson, H., & Marteinsdóttir, G. (2013). The circulation of icelandic waters–a modelling study. *Ocean Science*, *9* (5), 931–955.

Lozier, M. S., Li, F., Bacon, S., Bahr, F., Bower, A. S., Cunningham, S., ... others (2019). A sea change in our view of overturning in the subpolar North Atlantic. *Science*, *363* (6426), 516–521.

Martínez-Moreno, J., Hogg, A. M., England, M. H., Constantinou, N. C., Kiss, A. E., & Morrison, A. K. (2021). Global changes in oceanic mesoscale currents over the satellite altimetry record. *Nature Climate Change*, *11* (5), 397–403.

Mashayek, A., Gula, J., Baker, L., Garabato, A. N., Cimoli, L., & Riley, J. (2021). Mountains to climb: On the role of seamounts in upwelling of deep ocean waters.

Preprint(Version 1).

Mason, E., Pascual, A., & McWilliams, J. C. (2014). A new sea surface height–based code for oceanic mesoscale eddy tracking. *Journal of Atmospheric and Oceanic Technology*, *31*(5), 1181–1188.

McPhee, M. G. (1992). Turbulent heat flux in the upper ocean under sea ice. *Journal of Geophysical Research: Oceans*, *97*(C4), 5365–5379.

McPhee, M. G., & Martinson, D. G. (1994). Turbulent mixing under drifting pack ice in the Weddell Sea. *Science*, *263*(5144), 218–221.

Meehl, G. A., Goddard, L., Boer, G., Burgman, R., Branstator, G., Cassou, C., ... others (2014). Decadal climate prediction: an update from the trenches. *Bulletin of the American Meteorological Society*, *95*(2), 243–267.

Morrow, R., Fu, L.-L., Ardhuin, F., Benkiran, M., Chapron, B., Cosme, E., ... others (2019). Global observations of fine-scale ocean surface topography with the Surface Water and Ocean Topography (SWOT) mission. *Frontiers in Marine Science*, *6*, 232.

Napolitano, D. C., Carton, X., & Gula, J. (2024). Vertical interaction between nbc rings and its implications for south atlantic water export. *Journal of Geophysical Research: Oceans*, *129*(4), e2023JC020741.

Perkins, H., Hopkins, T., Malmberg, S.-A., Poulain, P.-M., & Warn-Varnas, A. (1998). Oceanographic conditions east of Iceland. *Journal of Geophysical Research: Oceans*, *103*(C10), 21531–21542.

Petit, T., Mercier, H., & Thierry, V. (2019). New insight into the formation and evolution of the East Reykjanes Ridge current and Irminger current. *Journal of Geophysical Research: Oceans*, *124*(12), 9171–9189.

Polyakov, I. V., Pnyushkov, A. V., Alkire, M. B., Ashik, I. M., Baumann, T. M., Carmack, E. C., ... others (2017). Greater role for atlantic inflows on sea-ice loss in the eurasian basin of the arctic ocean. *Science*, *356*(6335), 285–291.

Pörtner, H.-O., Roberts, D. C., Masson-Delmotte, V., Zhai, P., Tignor, M., Poloczanska, E., & Weyer, N. (2019). The ocean and cryosphere in a changing climate. *IPCC special report on the ocean and cryosphere in a changing climate*, *1155*.

Qu, L., Thomas, L., & Gula, J. (2021). Bottom mixing enhanced by tropical storm-generated near-inertial waves entering critical layers in the Straits of Florida. *Geo-*

physical Research Letters, *48*(15), e2021GL093773.

Renault, L., Masson, S., Arsouze, T., Madec, G., & McWilliams, J. C. (2020). Recipes for how to force oceanic model dynamics. *Journal of Advances in Modeling Earth Systems*, *12*(2), e2019MS001715.

Ruan, X., Wenegrat, J. O., & Gula, J. (2021). Slippery bottom boundary layers: The loss of energy from the general circulation by bottom drag. *Geophysical Research Letters*, *48*(19), e2021GL094434.

Saha, S., Moorthi, S., Pan, H.-L., Wu, X., Wang, J., Nadiga, S., ... others (2010). The NCEP climate forecast system reanalysis. *Bulletin of the American Meteorological Society*, *91*(8), 1015–1058.

Sarafanov, A., Falina, A., Mercier, H., Sokov, A., Lherminier, P., Gourcuff, C., ... Daniault, N. (2012). Mean full-depth summer circulation and transports at the northern periphery of the Atlantic Ocean in the 2000s. *Journal of Geophysical Research: Oceans*, *117*(C1).

Saunders, P. M. (1996). The flux of dense cold overflow water southeast of Iceland. *Journal of Physical Oceanography*, *26*(1), 85–95.

Schubert, R., Vergara, O., & Gula, J. (2023). The open ocean kinetic energy cascade is strongest in late winter and spring. *Communications Earth & Environment*, *4*(1), 450.

Shchepetkin, A. F., & McWilliams, J. C. (2005, January). The regional oceanic modeling system (ROMS): a split-explicit, free-surface, topography-following-coordinate oceanic model. *Ocean Modelling*, *9*(4), 347–404.

Shchepetkin, A. F., & McWilliams, J. C. (2011, January). Accurate Boussinesq oceanic modeling with a practical, "Stiffened" Equation of State. *Ocean Modelling*, *38*(1-2), 41–70. doi: 10.1016/j.ocemod.2011.01.010

Shi, J.-R., Santer, B. D., Kwon, Y.-O., & Wijffels, S. E. (2024). The emerging human influence on the seasonal cycle of sea surface temperature. *Nature Climate Change*, 1–9.

Strehl, A.-M., Våge, K., Smedsrud, L. H., & Barreyre, T. (2024). A 70-year perspective on water-mass transformation in the Greenland Sea: From thermobaric to thermal convection. *Progress in Oceanography*, *227*, 103304.

Su, Z., Wang, J., Klein, P., Thompson, A. F., & Menemenlis, D. (2018). Ocean submesoscales as a key component of the global heat budget. *Nature communications*, *9*(1), 775.

Tagliabue, A., Lough, A. J., Vic, C., Roussenov, V., Gula, J., Lohan, M. C., ... Williams, R. G. (2022). Mechanisms driving the dispersal of hydrothermal iron from the northern Mid Atlantic Ridge. *Geophysical Research Letters*, *49*(22), e2022GL100615.

Tchilibou, M., Carrere, L., Lyard, F., Ubelmann, C., Dibarboure, G., Zaron, E. D., & Arbic, B. K. (2025). Internal tides off the Amazon shelf in the western tropical Atlantic: analysis of SWOT Cal/Val mission data. *Ocean Science*, *21*(1), 325–342.

Thompson, A. F., Lazar, A., Buckingham, C., Garabato, A. C. N., Damerell, G. M., & Heywood, K. J. (2016). Open-ocean submesoscale motions: A full seasonal cycle of mixed layer instabilities from gliders. *Journal of Physical Oceanography*, *46*(4), 1285–1307.

Tsubouchi, T., Våge, K., Hansen, B., Larsen, K. M. H., Østerhus, S., Johnson, C., ... Valdimarsson, H. (2021). Increased ocean heat transport into the Nordic Seas and Arctic Ocean over the period 1993–2016. *Nature Climate Change*, *11*(1), 21–26.

Uchida, T., Le Sommer, J., Stern, C., Abernathey, R., Holdgraf, C., Albert, A., ... others (2022). Cloud-based framework for inter-comparing submesoscale permitting realistic ocean models. *Geoscientific Model Development Discussions*, *2022*, 1–32.

Ullgren, J. E., Fer, I., Darelius, E., & Beaird, N. (2014). Interaction of the Faroe Bank Channel overflow with Iceland Basin intermediate waters. *Journal of Geophysical Research: Oceans*, *119*(1), 228–240.

Van Aken, H., & Becker, G. (1996). Hydrography and through-flow in the northeastern North Atlantic Ocean: the NANSEN project. *Progress in Oceanography*, *38*(4), 297–346.

Verger-Miralles, E., Mourre, B., Gómez-Navarro, L., Barceló-Llull, B., Casas, B., Cutolo, E., ... others (2024). SWOT enhances small-scale intrathermocline eddy detection. *Authorea Preprints*.

Vic, C., Hascoët, S., Gula, J., Huck, T., & Maes, C. (2022). Oceanic mesoscale cyclones cluster surface Lagrangian material. *Geophysical Research Letters*, *49*(4), e2021GL097488.

Wang, J., Archer, M., Klein, P., & Fu, L.-L. (2025). Global Submesoscale Ocean Dynamics Unveiled by Wide-Swath Satellite Altimetry.

Winton, M., Griffies, S. M., Samuels, B. L., Sarmiento, J. L., & Frölicher, T. L. (2013). Connecting changing ocean circulation with changing climate. *Journal of climate*, *26*(7), 2268–2278.

Zhang, X., Liu, L., Fei, J., Li, Z., Wei, Z., Zhang, Z., ... Xu, F. (2024). Advances in surface water and ocean topography for fine-scale eddy identification from altimeter sea surface height merging maps. *EGUsphere*, *2024*, 1–19.

Zhang, Z., Miao, M., Qiu, B., Tian, J., Jing, Z., Chen, G., ... Zhao, W. (2024). Submesoscale eddies detected by SWOT and moored observations in the Northwestern Pacific. *Geophysical Research Letters*, *51*(15), e2024GL110000.

Zhao, J., Bower, A., Yang, J., Lin, X., & Penny Holliday, N. (2018). Meridional heat transport variability induced by mesoscale processes in the subpolar North Atlantic. *Nature communications*, *9*(1), 1124.

Zou, S., Bower, A., Furey, H., Susan Lozier, M., & Xu, X. (2020). Redrawing the iceland- scotland overflow water pathways in the north atlantic. *Nature communications*, *11*(1), 1890.

Zou, S., Lozier, S., Zenk, W., Bower, A., & Johns, W. (2017). Observed and modeled pathways of the Iceland Scotland Overflow Water in the eastern North Atlantic. *Progress in Oceanography*, *159*, 211–222.